Fine tuning the structural colours of photonic nanosheet suspensions by polymer doping

Karin El Rifaii, Henricus Herman Wensink, Claire Goldmann, Laurent Michot, Jean-Christophe P. Gabriel, Patrick Davidson

ARTICLE – PRE-PROOF VERSION

Fine tuning the structural colours of photonic nanosheet suspensions by polymer doping

Received 18th June 2021,
Accepted 29th September 2021

DOI: 10.1039/D1SM00907A

Karin El Rifaii,[a] Henricus H. Wensink,[*a] Claire Goldmann,[a] Laurent Michot,[b] Jean-Christophe P. Gabriel [*c] and Patrick Davidson[a]

Aqueous suspensions of nanosheets are readily obtained by exfoliating low-dimensional mineral compounds like $H_3Sb_3P_2O_{14}$. The nanosheets self-organize, at low concentration, into a periodic stack of membranes, i.e. a lamellar liquid-crystalline phase. Due to the dilution, this stack has a large period of a few hundred nanometres, it behaves as a 1-dimensional photonic material and displays structural colours. We experimentally investigated the dependence of the period on the nanosheet concentration. We theoretically showed that it cannot be explained by the usual DLVO interaction between uniform lamellae but that the particulate nature of nanosheet-laden membranes must be considered. Moreover, we observed that adding small amounts of 100 kDa poly(ethylene oxide) (PEO) decreases the period and allows tuning the colour throughout the visible range. PEO adsorbs on the nanosheets, inducing a strong reduction of the nanosheet charge. This is probably due to the Lewis-base character of the EO units of PEO that become protonated at the low pH of the system, an interpretation supported by theoretical modeling. Oddly enough, adding small amounts of 1 MDa PEO has the opposite effect of increasing the period, suggesting the presence of an additional intermembrane repulsion not yet identified. From an applied perspective, our work shows how the colours of these 1-dimensional photonic materials can easily be tuned not only by varying the nanosheet concentration (which might entail a phase transition) but also by adding PEO. From a theoretical perspective, our approach represents a necessary step towards establishing the phase diagram of aqueous suspensions of charged nanosheets.

1. Introduction

The controlled delamination in a solvent of layered crystalline materials, such as oxides, phosphates, graphite, II-VI compounds, or clays, is a widely used process to obtain colloidal suspensions of nanosheets.[1–24] By nanosheets, we mean thin disk-like nanoparticles of very small, monodisperse, thickness (t) and very large, polydisperse, diameter (D), with a well-defined in-plane crystallographic structure. Apart from their many industrial applications, like the ubiquitous uses of clays, these colloidal suspensions have recently raised much interest from a fundamental perspective as versatile model systems to explore the liquid-crystalline behaviour expected for particles of such high aspect ratio ($D/t \approx 100 - 1000$). Apart from the nematic phase which has often been reported,[25–38] the lamellar (or smectic) phase also sometimes occurs (Figure 1).[39–45] Interestingly, for highly charged nanosheets dispersed in polar solvents, the lamellar phase may appear at very high dilution, for nanosheet weight fractions below ≈ 1 wt%. Then, the lamellar period is similar to the wavelength range of visible light, which imparts these suspensions with a wide range of structural colours.[39,42] Moreover, depending on the precise chemical nature of the nanosheets, the structural colour of the suspensions varies upon exposure to different chemicals or physical stresses, which makes them good candidates for sensor applications.[46,47]

Although various hybrid liquid-crystalline systems comprised of nanosheets and polymers have already been investigated,[48–50] the influence of the addition of a neutral flexible polymer on the period of the lamellar phase of nanosheet suspensions has not been explored yet. In this work, we show how the lamellar period of $H_3Sb_3P_2O_{14}$ nanosheet suspensions can be decreased or increased at will by adding small amounts of poly(ethylene oxide) (PEO) of low or high molecular weight, which allows shifting the suspension structural colour, for example, from green to blue or from blue to green, respectively

Furthermore, we provide a detailed theoretical description of the dependence of the lamellar period on nanosheet concentration which, in contrast to previous work,[19,42] takes into account the particulate nature of the smectic layers (Figure 1). Indeed, upon dilution, the swelling of the lamellar phase is a complex process as both the lamellar period and the inter-particle distance within each layer may increase, which is an

[a] Laboratoire de Physique des Solides, Université Paris-Saclay, CNRS, 91405 Orsay, France.
[b] Laboratory of Physical Chemistry of Electrolytes and Interfacial Nanosystems (PHENIX), Sorbonne Universite', CNRS, 75005 Paris, France.
[c] Université Paris-Saclay, CEA,CNRS, NIMBE-LICSEN, 91191 Gif-sur-Yvette, France.

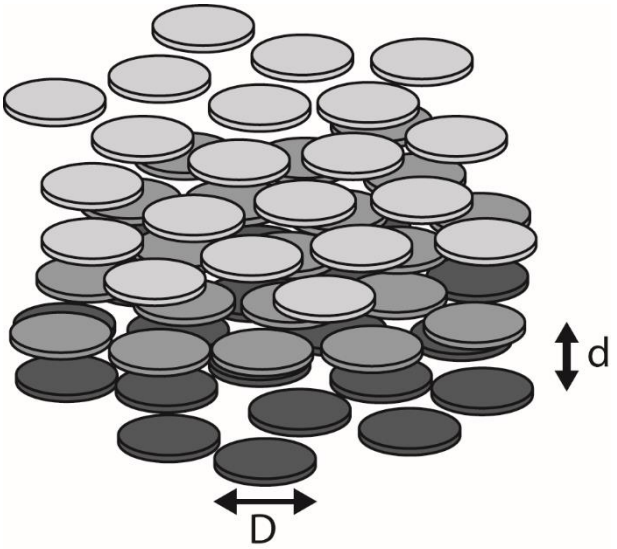

Fig. 1. Schematic organization of the lamellar phase of aqueous suspensions of $H_3Sb_3P_2O_{14}$ nanosheets (depicted as small disks gathered in equidistant layers). Nanosheets of the same grey shade belong to the same layer. d is the lamellar period and D is the nanosheet diameter.

issue has received limited attention thus far.[41,51] Hence, our theoretical description essentially captures the evolution of the structural colours with nanosheet concentration as well as with the addition of low molecular weight PEO.

This article is organized as follows: The next section provides experimental details. Section 3 describes and briefly discusses all experimental results obtained first with pure aqueous suspensions of $H_3Sb_3P_2O_{14}$ nanosheets, then with hybrid systems of nanosheets and PEO of low and high molecular weight. Section 4 deals with the theoretical modelling of the period of the lamellar phase, taking explicitly into account the particulate nature of the lamellae. Finally, in the conclusion (Section 5), we summarize our most salient results, comment on pending issues, and discuss ways to further improve the theoretical description.

2. Materials and Methods

2.1. Materials

$H_3Sb_3P_2O_{14}$ synthesis & characterization

$H_3Sb_3P_2O_{14}$ was synthesized according to a scaled-up procedure derived from a previously published method.[39,40] $K_3Sb_3P_2O_{14}$ was first synthesized using a stoichiometric mixture of $NH_4H_2PO_4$ (homemade, 0.224 mol, 25.823 g), Sb_2O_3 (MERCK, 0.166 mol, 48.367 g), and KNO_3 (PROLABO, 0.332 mol, 33.552 g) that was placed in a large platinum crucible and heated in air, up to 300°C (ramp: 50°C.h^{-1}) for 10 hrs to decompose $NH_4H_2PO_4$, then up to 1000°C (same ramp) for 24 hrs, yielding 83.633 g (0.109 mol; yield = 98.4%) of $K_3Sb_3P_2O_{14}$ (X-ray powder diffraction showed impurities level < 1%).

Then, a cationic exchange of $K_3Sb_3P_2O_{14}$ was performed to synthesize the final product, $H_3Sb_3P_2O_{14}$, using repeated acidic treatments as follows: 60.001 g of $K_3Sb_3P_2O_{14}$ powder was thoroughly ground and stirred in a 2 L solution of 7.5 N nitric acid at 50°C for 24 hrs. Then, the resulting white powder was recovered by centrifugation (4500 g) and immediately dispersed again in 2 L of 7.5 N nitric acid. This cation exchange procedure was overall repeated three times to ensure complete exchange of the alkali metal cations for protons, to yield $H_3Sb_3P_2O_{14}$. Finally, the white $H_3Sb_3P_2O_{14}$ powder was rinsed several times using absolute ethanol followed by material recovery by centrifugation.

A mother suspension of $H_3Sb_3P_2O_{14}$ was finally produced by: (1) dispersing 20 g of $H_3Sb_3P_2O_{14}$ into 1 L of 18 MΩ.cm water under strong agitation for 30 min; (2) centrifuging the suspension at 3600 g for 15 min; (3) collecting the supernatant. This last procedure allows removing traces of solid impurities as well as the largest size fraction of particles. Overall, ≈ 1 L of $H_3Sb_3P_2O_{14}$ opalescent suspension at 1.62 wt% was collected (81% yield). Its nitrate ion concentration was measured to be less than 1 ppm (JBL, nitrate test). The weight fraction of the $H_3Sb_3P_2O_{14}$ suspension was determined by thermogravimetric analysis under N_2 (TGA92 from SETARAM, Caluire, France) by heating to 250°C. The calcined material collected after TGA was white, showing the absence of any organic contamination. Moreover, scanning electron microscopy (SEM) experiments (see figure SI 1) have shown that the $H_3Sb_3P_2O_{14}$ nanosheets have an irregular shape, an average diameter <D> ≈ 1100 nm, in fair agreement with previous measurements (<D> ≈ 800 nm)[40], and a diameter polydispersity of about 70%. The thickness of the nanosheets was measured by AFM (see figure SI 2) to be 1.1 ± 0.1 nm, similarly to previously published values.

$H_3Sb_3P_2O_{14}$ nanosheet aqueous suspensions have a strong acidic character, leading to a pH of ≈ 1.5 at 1.62 wt%, which was already reported.[52] This corresponds to a negative nominal ("bare") surface charge density of 0.55 C.m^{-2}, a value that can also be inferred from the crystallographic structure of the solid-state compound.

The presence of a large negative charge on the nanosheets in aqueous suspension is qualitatively confirmed by the measurement of their zeta-potential (≈ -50 mV).

Most nanosheet / polymer mixtures were prepared with PEO of molar mass M_W = 100 kDa (average polymerization degree: 2300), purchased from Sigma-Aldrich. Additional experiments were also performed with PEO of 1 MDa M_W, as well as with dextran (a natural polysaccharide also purchased from Sigma-Aldrich) of 100 kDa M_W. The polydispersity distributions of these polymers were not determined by the provider.

2.2. Methods

Sample preparation

In order to investigate the 2-dimensional phase diagram represented in function of the nanosheet and polymer concentrations, $H_3Sb_3P_2O_{14}$ nanosheet and PEO mixtures were prepared by mixing directly the nanosheet suspensions with PEO solutions in deionized water. The composition of each sample was defined by the weight fractions, C_{H3} and C_{PEO}, of the $H_3Sb_3P_2O_{14}$ nanosheets and PEO, respectively. We use weight fraction in most of this work because the density of these

corrugated and somewhat porous nanosheets is not very precisely known. When absolutely required, for example, for comparison with the theory, we used a density of 4.2 g.cm^{-3}. All volumes were measured precisely by using a calibrated micropipette, the suspensions had the same 1.00 mL volume and were poured into 2 mL glass vials. The suspensions of $H_3Sb_3P_2O_{14}$ nanosheets are quite stable (for many years in the absence of PEO and for at least two years in presence of PEO), from the points of view of both chemical and colloidal stabilities. However, the structural colours slowly evolve during the first months after sample preparation but this evolution is almost over after three months. For this reason, most of the data shown in this article were obtained from three-month old samples.

Visual inspection of the samples

To assess the influence of doping $H_3Sb_3P_2O_{14}$ nanosheet suspensions with polymers, series of samples with constant C_{H3} or C_{PEO}, were examined in natural light and in polarized light (i.e. between crossed polarizers) to determine the number and nature of coexisting phases. A schematic representation of the setup used to observe the samples in polarized-light is shown in Figure SI 3. These observations were documented with an Olympus XZ-1 camera, using the flash at normal incidence.

SAXS experiments

The $H_3Sb_3P_2O_{14}$ / PEO (100 kDa) system was first investigated at the ID02 (Time-Resolved Ultra-Small-Angle X-Ray Scattering) beamline of the European Synchrotron Radiation Facility, in Grenoble, France.[53] The X-ray energy was 12.46 keV (wavelength $\lambda = 9.95 \times 10^{-2}$ nm), the sample-to-detector distance was 20.007 m, so that the scattering vector modulus, q ($q = (4\pi\sin\theta)/\lambda$ where 2θ is the scattering angle) ranges between 0.005 and 0.230 nm^{-1}. The beam size was 75 x 75 µm^2 at the sample level and the detector was a Frelon camera. The exposure time was typically 1.00 s.

Complementary SAXS measurements of the $H_3Sb_3P_2O_{14}$ / PEO (1 MDa) were made at the Swing SAXS beamline of the SOLEIL synchrotron radiation facility at Saint-Aubin, France. The X-ray energy was 12.0 keV, corresponding to the wavelength $\lambda = 0.1033$ nm, and a q-range between 10^{-2} and 1.0 nm^{-1}. The sample-to-detector distance was 6.226 m and the beam-size at the level of the sample was 375 x 75 µm^2. The exposure time was typically about 0.5 s. The scattering patterns were recorded with a Eiger-4 M detector.

In both cases, usual data reduction procedures were made and data were displayed either as 2-dimensional SAXS patterns or as plots of the scattered intensity versus scattering vector modulus, I(q), obtained by azimuthal averaging of the SAXS patterns. In first approximation, a quantity directly proportional to the structure factor, S(q), of the phase can simply be recovered by multiplying I(q) by q^2 (Kratky representation) since the particle form factor decays as q^{-2} in this q-range (called "intermediate" range).[54]

The samples were filled into cylindrical Lindemann glass capillaries of 1.0 ± 0.1 mm diameter (Glas-Technik & Konstruktion, Germany) and sealed with hot glue.

Thermogravimetric analysis (TGA)

TGA measurements (TGA92 from SETARAM, Caluire, France)) were performed under a N_2 atmosphere by heating samples up to 250°C at a rate of 1°C.min^{-1}, to determine the nanosheet weight fraction of the initial suspension batch, which was used to prepare all the samples described in this work. TGA was also used to determine the weight fractions of the coexisting phases in biphasic samples along a dilution line (in absence of polymer), for detailed comparison with the theory.

Adsorption isotherms

As PEO shows no peak in UV-vis-NIR light absorption spectroscopy, its adsorption isotherm on $H_3Sb_3P_2O_{14}$ nanosheets was obtained with a two-step, slightly involved, protocol already described in detail.[50] In a first step, the viscosity of 14 solutions of PEO (100 kDa) with different concentrations, ranging from 0 to 2.0 wt%, was measured using an Anton Paar automatic Microviscosimeter AMVn, producing a calibration curve relating viscosity with PEO concentration. The second step was to mix 0.5 ml of each of these solutions with 2.0 ml of an $H_3Sb_3P_2O_{14}$ suspension at C_{H3} = 1.6 wt%. After 16 hours, the suspensions were centrifuged at 105 000 g, and the viscosity of the supernatant was measured. Then, the remaining PEO content could be deduced, based on the calibration curve. The adsorbed amount was then obtained by the relation $Q_a = (V/M)(c_i - c_e)$ where c_i and c_e are the initial and equilibrium concentrations in PEO, respectively, V the suspension volume, and M the mass of solid in the suspension.

Zetametry

Electrophoretic measurements were carried out using a Zetasizer Nano ZS (Malvern) at a wavelength of 632 nm in a folded capillary polycarbonate cell, with gold electrodes, that contains ≈ 1 ml of suspension. The applied potential was set around 150 V. The electrophoretic mobility was measured at 25°C. If required, the contribution of the PEO to the solvent viscosity was taken into account by using the values measured previously with the microviscosimeter. The data was averaged over two sets of measurements.

3. Experimental results and discussion

3.1. Dilution of the $H_3Sb_3P_2O_{14}$ lamellar phase

Dilution with water has a remarkable influence on the $H_3Sb_3P_2O_{14}$ lamellar phase, as illustrated in Figure 2. Indeed, the structural colour of the phase gradually evolves from blue to red, which suggests that the lamellar period increases with decreasing concentration.

Moreover, observation of the samples between crossed polarizers reveals that the proportion of lamellar phase in the sample gradually decreases upon increasing dilution. This latter observation is expected because, briefly, first-order phase transitions occur from the lamellar phase to a nematic phase

and then to the isotropic phase (see reference [40] for more details on the polymorphism of these suspensions). Presumably, the increase of lamellar period with decreasing concentration is a consequence of the nanosheet diameter dispersity, in which case the concentration and composition of the lamellar phase (and of the coexisting nematic) both change upon traversing the biphasic gap.

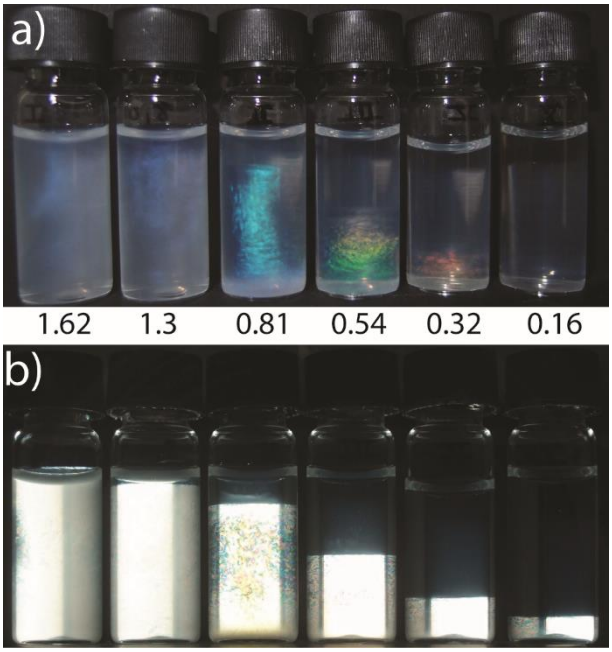

Fig. 2 Photographs of a series of sample tubes with weight fraction of $H_3Sb_3P_2O_{14}$ decreasing from left to right : c_{H3}= 1.62, 1.30, 0.81, 0.54, 0.32, and 0.16 wt% observed a) in natural light: the structural colour changes upon sample dilution and b) between crossed polarizers where the proportion of birefringent phase decreases with c_{H3}. The birefringent phase appears at the bottom of the samples because it is denser than the isotropic phase.

These observations and conclusions are confirmed by a small-angle X-ray scattering investigation of the samples (Figure 3). The SAXS patterns of the lamellar phase show very sharp diffraction features (rings and/or spots) that arise from its (quasi-)long-range 1-dimensional positional order. The corresponding scattered intensity, I(q), (azimuthal averaging of the pattern, see Materials and Methods section) shows equidistant sharp diffraction peaks. The lamellar period, d, is related to the position, q_0, of the first-order diffraction peak by $d = 2\pi/q_0$.

The lamellar periods measured by SAXS are consistent with the structural colours of the samples assessed from photographs recorded with the flash of the camera (i.e. in reflection, at normal incidence). The wavelength λ of the structural colour diffracted by a layered composite material at normal incidence is simply given by $2nd = \lambda$ where n is the refractive index of water and the nanosheet thickness was neglected in front of the lamellar period.[55] For example, the samples with C_{H3} = 0.81, 0.54, and 0.32 wt%, respectively have lamellar periods of 167, 200, and 224 nm, corresponding to diffracted light of wavelength 444, 532, and 596 nm, which is consistent with their respective blue, green, and red structural colours (Fig. 2a).

The dependence of the lamellar period on the nanosheet concentration will be discussed in more detail below (Section 4).

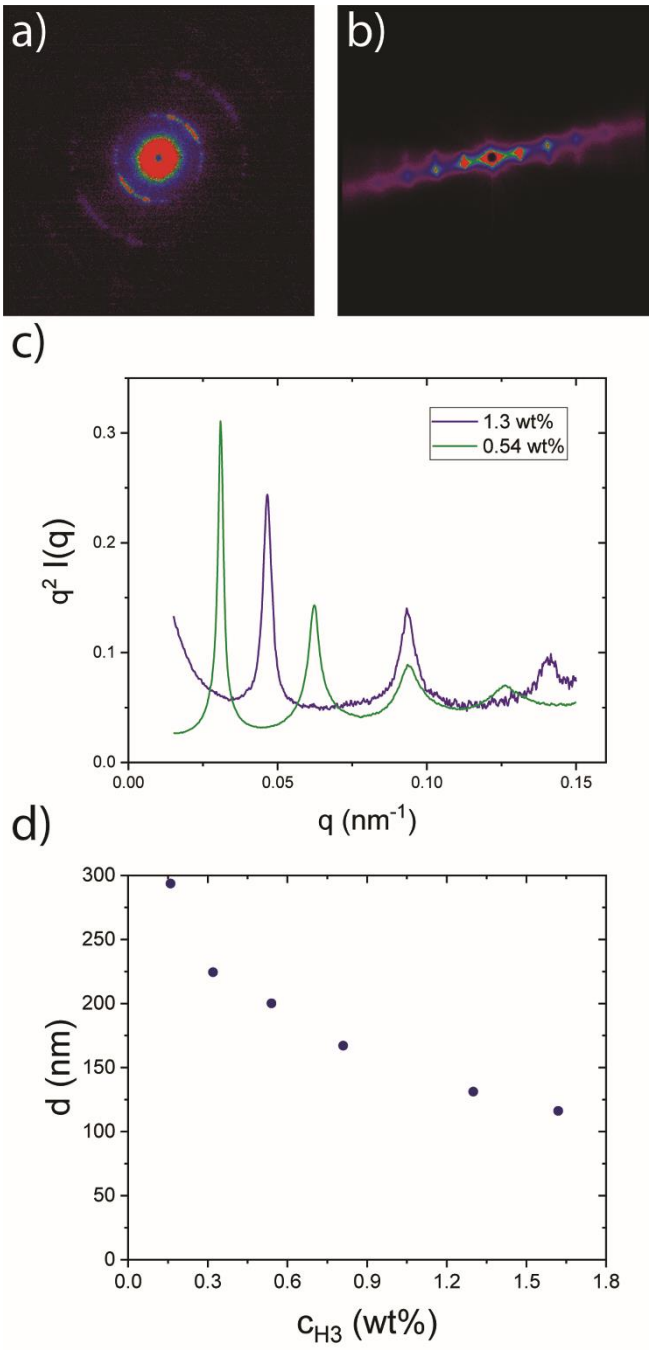

Fig. 3 SAXS investigation of the samples shown in Figure 2. SAXS patterns of the lamellar phase a) for the most concentrated sample with C_{H3}=1.3 wt% and b) a diluted sample with C_{H3}=0.54 wt%, c) the corresponding curves of azimuthally-averaged scattered intensity in Kratky representation, and d) the dependence of the lamellar period on the nanosheet weight fraction.

3.2. The $H_3Sb_3P_2O_{14}$ / PEO system

3.2.1. PEO of molecular weight 100 kDa

The most striking effect of PEO (100 kDa) addition to the suspensions of $H_3Sb_3P_2O_{14}$ nanosheets is a change of their structural colours (Figure 4a). For example, the lamellar phase of a $H_3Sb_3P_2O_{14}$ biphasic nanosheet suspension at C_{H3} = 0.32 wt% shows, in natural light at normal incidence, a red colour in the absence of PEO, but it turns green at C_{PEO} = 0.5 wt% and then blue at C_{PEO} = 2.0 wt%. This colour change strongly suggests that the lamellar period progressively decreases upon PEO addition. The observation of the samples between crossed polarizers (Figure 4b) shows that they remain biphasic and that the proportion of their birefringent part first remains almost constant until it slightly decreases at high polymer doping. This means that the liquid-crystalline phase is only marginally destabilized with respect to the isotropic one.

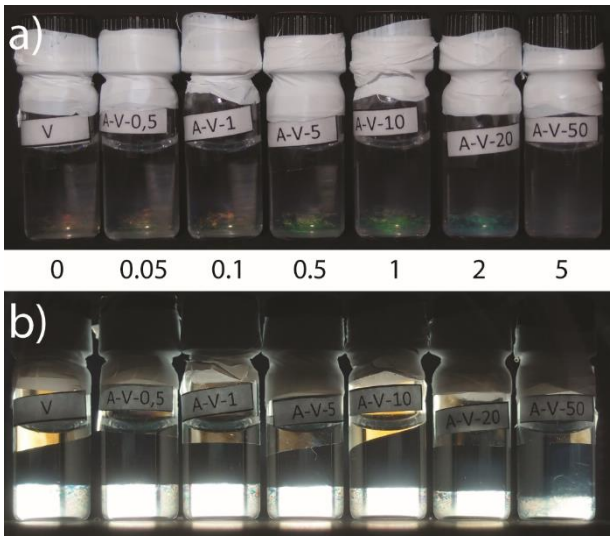

Fig. 4 Photographs of a series of sample tubes, with constant C_{H3} = 0.32 wt% and PEO weight fraction increasing from left to right: C_{PEO} = 0, 0.05, 0.1, 0.5, 1, 2, and 5 wt%, observed a) in natural light: the structural colour changes from red to blue due to PEO doping, and b) between crossed polarizers: the birefringent phase is barely destabilized.

These observations were confirmed by a synchrotron high-resolution SAXS investigation. Even doped with PEO, the pattern of the lamellar phase (Figure 5a) shows a series of equidistant diffraction peaks, which is again its classical signature.[40]

The measurements by SAXS of the lamellar period of six series of samples of constant $H_3Sb_3P_2O_{14}$ nanosheet concentration but increasing PEO doping are gathered in Figure 5b). The most salient feature is that the lamellar period decreases with increasing PEO doping, particularly so at the lowest nanosheet concentrations. For example, at the lowest concentration (C_{H3} = 0.16 wt%), the lamellar period decreases by 40% when C_{PEO} increases from 0 to 2.0 wt%. Another example is shown in Figure SI 4. The fact that the lamellar period is hardly affected by PEO doping for the most concentrated samples is reminiscent of the behaviour of lamellar phases of homogeneous surfactant membranes. At high overall concentration, nanosheet crowding within each lamella is considerable such that the particles are tightly packed together. Conservation of mass then dictates that the lamellar period

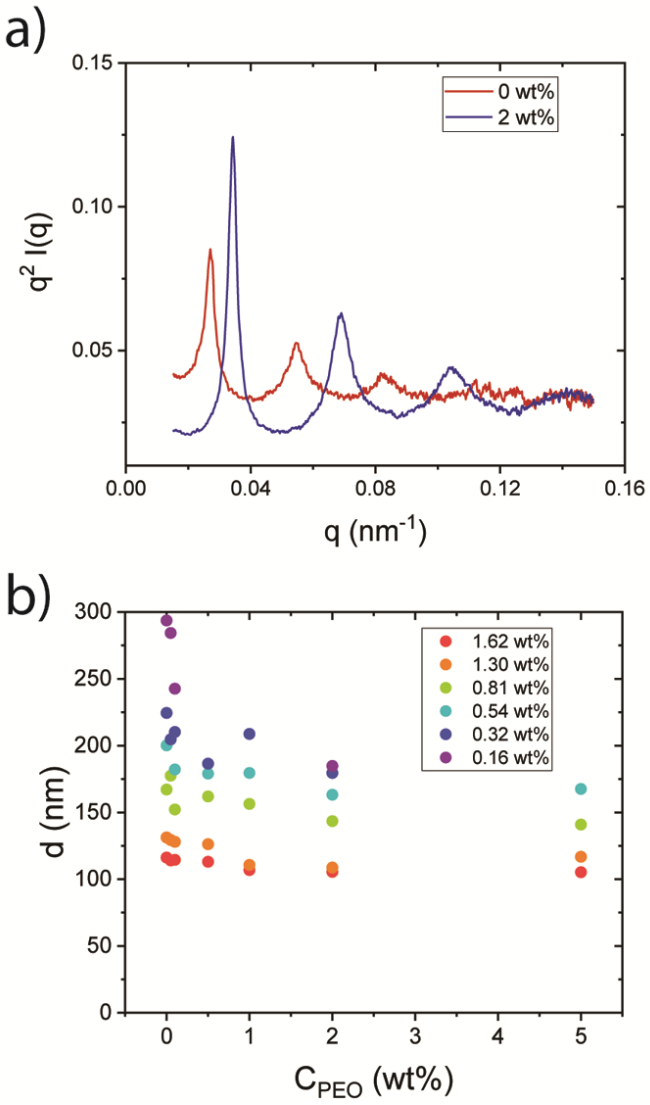

Fig. 5 a) Curves of azimuthally-averaged scattered intensity in Kratky representation, q2.I(q) versus q, of two samples with same nanosheet weight fraction, C_{H3} = 0.32 wt%, but different PEO weight fractions: 0 and 2 wt%. b) Dependence of the lamellar period on the PEO weight fraction for six series of samples with constant $H_3Sb_3P_2O_{14}$ weight fractions.

follow a simple swelling law defined by $d = \delta/\phi$ where δ is the membrane thickness (here the nanosheet thickness) and ϕ is the membrane volume fraction, which both remain constant upon PEO addition. This scenario will be discussed in paragraph 4.4 (Figure 10).

The structural colours displayed by the $H_3Sb_3P_2O_{14}$ / PEO samples (Figure 4a) are also consistent with the lamellar periods measured by SAXS (Figure 5b). Using Bragg's law, as in section 3.1 above, for the diffraction of light by a lamellar composite system, we find very good agreement between the lamellar periods and the structural colours of the samples For instance, for two samples with C_{H3} = 0.32 wt% and C_{PEO} = 0 and 5 wt% respectively, the lamellar periods measured by SAXS are 224.5 and 179.5 nm, corresponding to diffracted light of wavelength respectively 597 and 477 nm, and therefore orange and light-blue structural colours (see Fig. 4a).

The phase diagram of the $H_3Sb_3P_2O_{14}$ / PEO (100 kDa) system (Figure SI 5), as function of C_{H3} and C_{PEO}, has a biphasic region that tilts towards higher nanosheet concentration as C_{PEO} increases. Indeed, both liquid-crystalline lamellar and nematic phases are slightly destabilized with respect to the isotropic phase upon PEO doping. However, this effect is not much pronounced, even at the highest PEO concentration explored, which cannot exceed the solubility of PEO in water. In comparison, a much stronger destabilizing effect has been recently reported when PEO was added to the nematic phase of beidellite clay suspensions.[50]

Interestingly, we observed the same change of structural colour, due to a decrease of lamellar period upon addition of dextran polymer coils of 100 kDa molecular weight (see Figures SI 6 and SI 8). Dextran is a polysaccharide and therefore has a molecular structure quite different from that of PEO. This shows that the phenomenon described here is not restricted to the case of PEO and is not specific.

A study of PEO (100 kDa) adsorption on $H_3Sb_3P_2O_{14}$ nanosheets shows that PEO has in fact some affinity for the nanosheets, as illustrated by the PEO adsorption isotherm (Figure 6). The curve of PEO adsorption regularly increases until it saturates to an average value of ≈ 0.1 g adsorbed PEO per g of $H_3Sb_3P_2O_{14}$. This value is lower but still of the same order of magnitude as that recently reported for the adsorption of the same 100 kDa PEO on beidellite clay.[50] This saturated value corresponds to about 3000 PEO coils adsorbed on each nanosheet (1500 per side). Since the gyration radius, R_g, of PEO is about 25 nm,[56,57] the saturation value would roughly correspond to three times the full coverage if independent Gaussian coils were considered. Moreover, PEO bridging conformations also seem improbable because the average distance between nanosheets is 100 – 300 nm, which is much larger than the end-to-end distance of the polymer, while the elastic penalty for stretching is $\approx k_BT\,(d/R_g)^2$ where k_B is the Boltzmann constant and T the temperature.[58] Then, the PEO is likely to be adsorbed as tails,

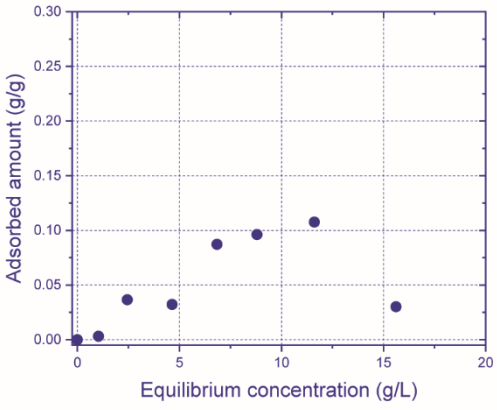

Fig. 6 Adsorption isotherm of PEO (100 kDa) on $H_3Sb_3P_2O_{14}$ nanosheets showing the adsorbed mass of PEO per gram of $H_3Sb_3P_2O_{14}$ versus the PEO concentration in the solution.

adsorbed trains, and loops at the surface of the nanosheets.[59]

Zetametry measurements (Figure 7) of the $H_3Sb_3P_2O_{14}$ / PEO samples provide information about the evolution of the surface charge density of the nanosheets upon PEO addition. We only qualitatively discuss here the evolution of the zeta potential upon PEO addition because the absolute values are computed by the apparatus software from the measured electrophoretic mobilities by assuming a spherical shape for the nanoparticles, which is not the case here at all. Qualitatively, nevertheless, the zeta potential of the nanosheets, which is negative, decreases regularly as the PEO concentration in the mixtures increases. This means that the surface charge density of the nanosheets clearly decreases as the PEO doping increases.

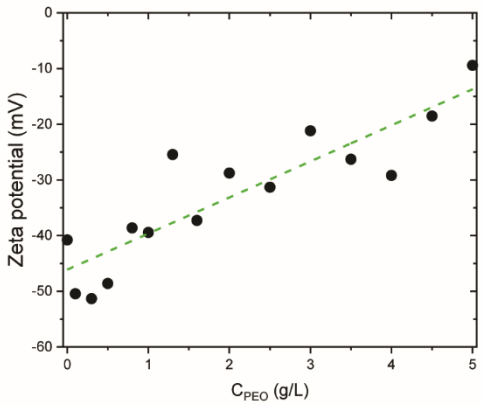

Fig. 7 Dependence of the zeta potential of $H_3Sb_3P_2O_{14}$ nanosheets versus PEO doping. The straight line is just a guide to the eye.

A possible explanation of this behaviour is based on the Lewis-base character of the ether oxygens of PEO which has been emphasised several times in the literature to explain its adsorption properties.[60,61] Indeed, the pH of a PEO aqueous solution reaches values ≈ 8 at C_{PEO} = 2.0 wt% (see Figure SI 7). In a $H_3Sb_3P_2O_{14}$ nanosheet suspension with pH ≈ 2, the ethylene oxide repeat units of PEO, which are Lewis bases, could be protonated, which would impart a positive electric charge to the polymer. This could explain the adsorption of PEO on the nanosheets which are negatively-charged and the strong reduction of zeta potential of the nanosheets after PEO adsorption. We note that dextran, whose addition also decreases the lamellar period, happens likewise to be regarded as a Lewis base (see Figure SI 9) in the literature.[62]

3.2.2. PEO of molecular weight 1 MDa

The behaviour of the lamellar phase of $H_3Sb_3P_2O_{14}$ doped with PEO of high molecular weight seems to be at odds with that described above with low molecular weight PEO or dextran. Indeed, Figure 8a shows that the structural colour of the lamellar phase shifts from blue to green upon addition of PEO (1 MDa), which suggests that the lamellar period increases with PEO content. Moreover, the lamellar phase is very slightly stabilized with respect to the isotropic phase (Figure 8b), in contrast with the case of PEO (100 kDa) shown in Figure 4b.

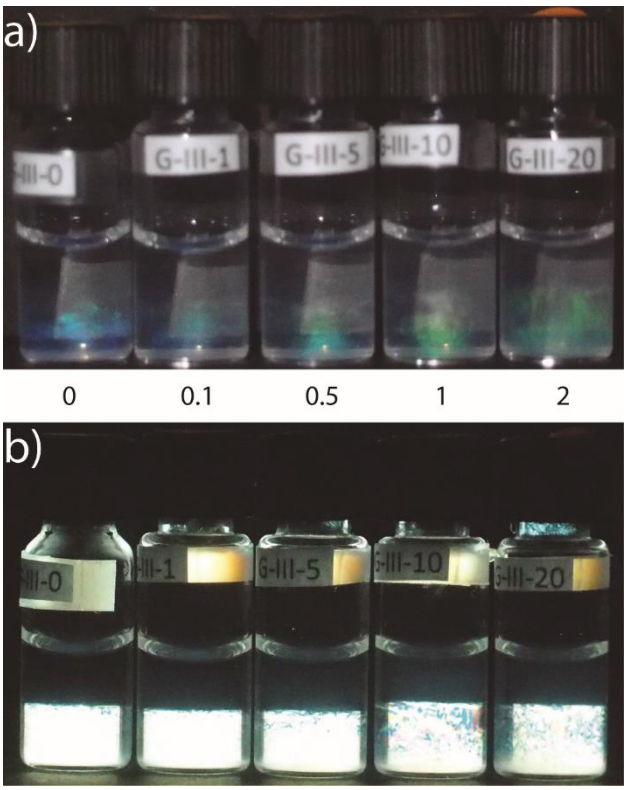

Fig. 8 Photographs of a series of sample tubes with constant C_{H3} = 0.54 wt% and PEO (1 MDa) weight fraction increasing from left to right: C_{PEO} = 0, 0.1, 0.5, 1, and 2 wt% observed a) in natural light: the structural colour changes from blue to green due to the PEO (1M) doping, and b) between crossed polarizers: the birefringent phase is barely stabilized with respect to the isotropic phase.

The SAXS study (Figure 9) of these samples confirms the conclusion that the addition of small amounts of PEO of high molecular weight does not alter the lamellar phase, apart from a small increase of its lamellar period.

This behaviour strongly suggests that the addition of high molecular weight PEO induces an additional repulsive interaction between the nanosheets. Since the Lewis-base character of the ether oxygens of PEO is most probably independent of its molecular weight, we still expect the PEO (1 MDa) to bear a positive electric charge at pH = 2. It should then adsorb on the nanosheets and therefore reduce their negative electric charge and electrostatic repulsions, as PEO (100 kDa) does. However, the gyration radius of PEO 1 MDa is approximately 100 nm, which is comparable to the period of the lamellar phase of the nanosheets. We therefore argue that the increase of the lamellar period upon addition of PEO (1 MDa) could be due to a soft steric repulsion related to the loops and tails of the partially adsorbed PEO coils.

4. Theory of lamellar order of charged nanosheets

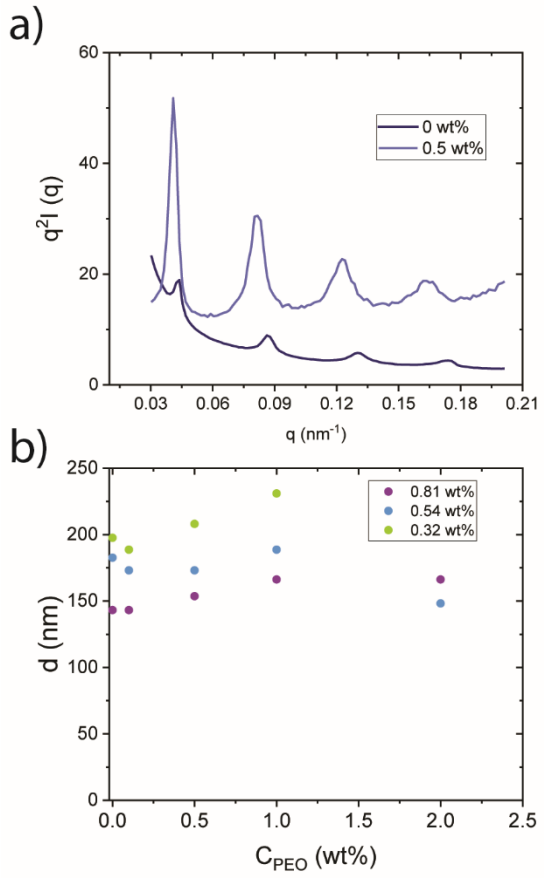

Fig. 9. a) SAXS curves of azimuthally-averaged scattered intensity in Kratky representation of three samples with constant C_{H3} = 0.81 wt% with and without addition of PEO (1 MDa) (C_{PEO} = 0 and 0.5 wt%) b) Dependence of the lamellar period on the PEO (1 MDa) doping.

In this section, we try to model the lamellar phase of charged nanosheets and to account for the dependence of the lamellar period first on the nanosheet volume fraction (Sections 4.1-4.4) and then on the PEO doping through a variation of the nanosheet charge (Section 4.5).

4.1. Modified DLVO theory for bilamellar system

Let us first attempt to predict the typical lamellar distance of the nanosheets by interpreting the lamellae as uniform layers of thickness *h* at a distance *d*. First, we consider the typical van der Waals energy between two such lamellae. In view of the large distance (*d* >> 10 nm), retardation effects are expected to be significant. Considering a retarded van der Waals potential $U = -C_r/r^7$ between atoms at center-of-mass distance *r* and performing a pairwise summation over atoms between two lamellae of density ρ, we find that the energy per unit area reads:[63]

$$\frac{U_{vdW}}{A} = \frac{-C_r \pi \rho^2}{30}\left\{\frac{1}{d^3} - \frac{2}{(d+h)^3} + \frac{1}{(d+2h)^3}\right\} \quad (1)$$

Taking the limit *h* << *d*, we find that the van der Waals term decays as the fifth power of the lamellar distance:

$$\frac{U_{vdW}}{A} \sim -4B\,\frac{h^2}{d^5} \quad (2)$$

where $B = \pi\rho^2 C_r/10$ refers to the retarded Hamaker constant which needs to be evaluated from Lifschitz theory. In fact, since the lamellae interact through aqueous medium, an effective Hamaker constant $B_{LWL} = B_{LL} + B_{WW} - 2B_{LW}$ should be considered with "*L*" referring to the lamellae and "*W*" to water. The retarded Hamaker constant (in vacuum) should typically be of the order $B \approx 10^{-28}$ J.m. We stress that this value might be quite different for two surfaces of material (possibly polymer-coated) immersed in water.

As for the electrostatic repulsion between lamellae, we note that the bare charge density on the nanosheet surface is very high ($\sigma \approx 3.4$ e/nm^2). The presence of ionic impurities in the solvent, on top of the H^+ counter-ions, act as added salt with a small but non-zero concentration $n_s \approx 10^{-5}$ M and corresponding Debye screening length of $\lambda_D \approx 100$ nm. Due to the high surface charge, the degrees-of-freedom of the ions in solution are strongly affected by the charged surface, as reflected by a coupling constant being much larger than unity ($\Xi = \ell_B/\ell_{GC} \approx 10$). This situation gives rise to strongly non-linear effects such as counter-ion condensation onto the nanosheet surface which can be accounted for from the non-linear Poisson-Boltzmann (PB) equation.[63]

Approximate analytical solutions exist for the simple bilayer geometry under certain circumstances.[64] Our bilayer system clearly operates in the so-called intermediate regime characterized by large interlamellar distances ($d/\lambda_D \gg 1$) and a very small Gouy-Chapman length ($\ell_{GC} \approx 0.067$ nm so that $\ell_{GC}/\lambda_D \ll 1$). The osmotic pressure between two charged walls with respect to a reservoir of pure electrolyte takes the following approximate form:[64]

$$\Pi_{int} \sim \frac{8k_BT}{\pi l_B \lambda_D^2}\exp\left(\frac{-d}{\lambda_D}\right) \quad (3)$$

in terms of the Bjerrum length $\ell_B \approx 0.67$ nm at room temperature. We remark that the current theory deviates somewhat from the conventional DLVO model for colloidal stability where retardation effects are usually ignored and electrostatic interactions between colloidal particles are treated at the level of linearized PB or Debye-Hückel theory.

Equilibrium lamellar distance

Combining the van der Waals and electrostatic pressures gives the total (disjoining) osmotic pressure between two charged lamellae:

$$\Pi \sim \frac{8k_BT\exp\left(\frac{-d}{\lambda_D}\right)}{l_B\lambda_D^2} - 20B\frac{h^2}{d^6} \quad (4)$$

The osmotic pressure is measured against a reservoir of ideal electrolyte. Then, taking $\Pi = 0$ and using the values specified thus far, we find maximum swelling with a typical lamellar distance of about $d^* \approx 35\lambda_D \approx 3500$ nm which is more than an order of magnitude larger than the typical lamellar spacing $d^* \approx 300$ nm found in experiment. Parameter variation within reasonable limits does not markedly change the interlamellar distance.

The discrepancy with the experimental value for lamellar phases becomes less striking when we realize that the lamellar phase is in fact composed of a stack of membranes in osmotic equilibrium with an isotropic (or nematic) fluid phase (F) of charged discs. In that case, we should set $\Pi = \Pi_F > 0$ with the latter being the pressure of the fluid suspension relative to the electrolyte reservoir pressure. Furthermore, the number density of discs may not be equal in both phases and particle exchange is allowed to happen such that the chemical potential $\mu = (F + \Pi V)/N$ is equal in the coexisting fluid and lamellar phases ($\mu_L = \mu_F$).

4.2. Nanosheet-laden lamellae

In order to arrive at a more appropriate description of the lamellar system under consideration, we must realize that the lamellae do not consist of a uniform material but are of a particulate nature, i.e. they are composed of strongly aligned rigid nanosheets with a very disperse diameter D with average $\langle D \rangle$ = 800 nm organized into a quasi-bidimensional fluid. The subtle balance between the average nanosheet distance along and transverse to the sheet normal (or nematic director) has been addressed previously in the context of Poisson-Boltzmann cell theory that was mainly applied to non-lamellar laponite clays.[65,66] Let us denote $\phi_\perp = (\pi/4)\,\rho_\perp D^2$ as the average bidimensional filling fraction of discs in each lamella, with $\rho_\perp$ the corresponding intralamellar number density. Since $\phi_\perp < 1$, we may associate to this an effective surface charge density that is smaller than the bare one:

$$\sigma_{eff} \sim \phi_\perp\,\sigma_{bare} \quad (5)$$

where we reiterate that $\sigma_{bare} \approx 0.55$ C/m^2. If we further take a typical intralamellar packing fraction $\phi_\perp = 0.5$, we find an effective Gouy-Chapman length:

$$l_{GC}^{eff} = \frac{e}{2\pi l_B |\sigma_{eff}|} \approx 1nm \quad (6)$$

We conclude that the effective Gouy-Chapman length remains about two orders of magnitude smaller than the Debye screening length ($\lambda_D \approx 100$ nm). This means that the interlamellar electrostatics continues to reside in the intermediate regime with the asymptotic pressure given by Eq. (3). In the Supplementary Information (Figure SI 10), we compare the disjoining pressure associated with Eq. (3) to the one obtained from a numerical solution of the nonlinear PB equation and find that the analytical form performs well for $\lambda_D/\ell_{GC} > 100$, provided that the interlamellar distance remains large ($d > \lambda_D$). Overall, Eq. (3) tends to give a slight overestimation of the disjoining pressure at large distance while underestimating the numerical result at shorter lamellar distances. Moreover, lamellar undulations are expected to be strongly suppressed given that the individual $H_3Sb_3P_2O_{14}$ nanosheets that make up the membrane are supposed to be rather rigid. Furthermore, since the lamellar distance is of the same order as the typical Debye length, the effect of the (long-wavelength) membrane fluctuations on the electrostatic interlamellar forces is expected to be negligible.[67–69]

From bilayer to multistack lamellae

A lamellar phase is composed of M lamellae which we assume to have identical physicochemical properties. Let us ignore the van der Waals contribution which is likely to be unimportant for the thermodynamics. For the Debye-Hückel regime (low effective surface charge density), one can show that the energy stored in each lamella is negligible if $h >> d$ (ϵ_L/ϵ_W) so that both sides of the membrane can be considered electrically independent.[70,71] If we consider this to hold for the intermediate regime as well, then by assuming pairwise additivity among lamellae, we can express the excess (over ideal) free energy of the lamellar phase (henceforth labelled "L") in terms of a sum of M - 1 independent bilayer systems:

$$F_L^{ex} \sim A(M-1)\frac{8k_BT}{\pi l_B \lambda_D}\exp\left(\frac{-d}{\lambda_D}\right) \quad (7)$$

Conservation of the total number of nanosheets implies that $N = \rho_L (M\text{-}1)Ad$. Since the nanosheet thickness is negligible compared to the lamellar distance d, the total particle number density is trivially connected to the intralamellar distance via $\rho_L = \rho_\perp/d$. We thus obtain for the interlamellar free energy:

$$\frac{F_L^{ex}}{Nk_BT} \sim \frac{8/\pi}{\rho_L d l_B \lambda_D}\exp\left(\frac{-d}{\lambda_d}\right) \quad (8)$$

The fact that the free energy per particle drops with the overall nanosheet concentration ρ_L is a direct consequence of the extremely high lamellar surface charge density. In the intermediate regime, the interlamellar repulsion is simply saturated and no longer depends on the surface charge density itself. This means that adding nanosheets to a lamella at fixed distance d does not enhance the interlayer repulsion, so that the free energy per particle drops.

Alternatively, if we assume each lamella to interact with all its neighbours, then we may naively sum Eq. (3) over all $M(M\text{-}1)/2$ lamellar pairs:

$$\frac{F_L^{ex}}{k_BT} \sim \frac{8A}{\pi l_B \lambda_D}\sum_{i=1}^{M-1}\sum_{j=i+1}^{M}\exp\left(-\frac{d(j-i)}{\lambda_D}\right) \quad (9)$$

Taking the limit $M \to \infty$ leads to:

$$\frac{F_L^{ex}}{Nk_BT} \sim \frac{8/\pi}{\rho_L d l_B \lambda_D}\left[\exp\left(\frac{d}{\lambda_D}\right)-1\right]^{-1} \quad (10)$$

which reduces to Eq. (8) for large lamellar separations $d >> \lambda_D$ as should be the case.

4.3. Thermodynamics of the intralamellar fluid

So far, we have not addressed the issue that each lamella exerts a lateral osmotic pressure (i.e., perpendicular to the lamellar direction) arising from the thermal motion of the discs across the lamellar plane. For simplicity, the nanosheets are considered to be parallel to each other, i.e., the orientational degrees of freedom are frozen. The free energy of a planar nanosheet fluid of which each lamella is composed can formally be established from liquid-state theory with the help of the direct correlation function $c_2(r)$. Rather than resorting to numerical strategies based on integral equation theory to resolve the intralamellar fluid structure, which is further compounded by the considerable diameter dispersity of the particles, we opt here for a naive but analytically tractable approach. We decouple the correlations between nanosheets into a hard-core contribution from Scaled Particle Theory[72,73] combined with a mean-field expression for the electrostatic part.[74] Furthermore, the sheets are assumed to be in a fluid state without long-ranged positional order across the lamellar plane. Experimental scattering data suggests that the intralamellar fluid structure to be very weak because no interference peak is observed in the plane perpendicular to the row of lamellar reflections in SAXS patterns of single domains of the lamellar phase.[40] The one-body density then reads $\rho(\mathbf{r}_\perp) = \rho_\perp$ with $\rho_\perp$ the bidimensional concentration of nanosheets in each lamella. The following expression for the excess (over ideal) free energy ensues:

$$\frac{F_{intra}^{ex}}{N} \sim \frac{1}{2}\rho_\perp \int_0^\infty 2\pi r_\perp U(r_\perp) g(r_\perp) dr_\perp + k_BT\left(\frac{1}{1-\phi_\perp} - \ln(1-\phi_\perp)\right) \quad (11)$$

where $g(r_\perp)$ denotes the intralamellar radial distribution function, as per the virial theorem.[74] Here, we approximate it by the expression $g(r_\perp) = H(r_\perp - \sigma)$ which ignores fluid structure beyond simple hard-core exclusions between nanosheet pairs, with H(x) denoting a Heaviside step function and σ some effective hard-core diameter. The latter is naturally related to D but it shall be retained here as an adjustable parameter since it is intricately affected by the nanosheet size dispersity as well as by details of the intralamellar fluid structure, both of which we

do not treat further here. The average distance between the mass centers of the nanosheets residing in a single lamella can be rather large, which suggests the use of Debye-Hückel far-field approximation for the pair interaction between nanosheets, provided the bare charge surface is replaced by a much smaller *effective* charge:[75]

$$\frac{U}{k_BT} \approx 4l_BZ_{eff}^2 \left(\frac{I_1(y\sin\theta')}{y\sin\theta'}\right)\frac{e^{-r/\lambda_D}}{D} \quad (12)$$

With I_1 denoting a modified Bessel function with argument y = (1/2) D/λ_D and θ denoting the angle between the disc normal and center-of-mass distance vector. Note that $\theta = \theta' = \pi/2$ for co-planar parallel discs. The prefactor features an effective charge Z_{eff} and a shape factor specific to the discotic colloidal shape. For highly charged discs, the saturation value for the effective surface charge is independent of the surface charge itself and takes the following scaling form:[75]

$$Z_{eff}^{sat} \approx \frac{D}{l_B}y \sim 5.10^3 \quad (13)$$

which is about three orders of magnitude smaller than the bare number of charges ≈ 10^6 per nanosheet. The integral in Eq. (11) is easily solved to obtain the following compact expression for the total intralamellar free energy:

$$\frac{F_{intra}^{ex}}{Nk_BT} \sim \pi l_B\lambda_D\omega_L\rho_L d + \frac{1}{1-\phi_\perp} - \ln(1-\phi_\perp) \quad (14)$$

The intralamellar repulsion amplitude ω_L combines various characteristics pertaining to the effective charge, shape, and intralamellar fluid structure of the nanosheets:

$$\omega_L = 4\,Z_{eff}^2\left(\frac{I_1(y)}{y}\right)^2 \exp\left(\frac{-\sigma}{\lambda_D}\right) \quad (15)$$

If we take $\sigma \approx D$, we find that the amplitude should be of the order $\omega_L \sim \mathcal{O}(10^6)$. It should be understood that an appropriate estimate of ω_L remains elusive in view of the approximate nature of the effective charge, at least for the intralamellar configurations considered here, and because of our cavalier treatment of the fluid structure which is strongly impacted by the considerable diameter dispersity of the nanosheets.

We further note that the intralamellar free energy increases with lamellar distance given that the lamellae get more crowded as more particles need to be accommodated in the layers when d increases at fixed particle density. Furthermore, the free energy diverges as the nanosheets reach close packing $\phi_\perp \to 1$ (in fact, actual close packing happens at $\phi_\perp = \pi\sqrt{3}/6 \approx 0.907$). The hard-core contribution provides a natural upper bound for the lamellar spacing set by the overall nanosheet concentration, $d_{max}/D \leq (\pi/4)(\rho_LD^3)^{-1}$. This we will discuss next.

4.4. Lamellar spacing versus nanosheet concentration

Combining the inter- and intra-lamellar electrostatic free energies and minimizing with respect to *d* we obtain a criterion for (mechanical) stability of the lamellar distance:

$$\frac{\partial}{\partial d}\left(F_L^{ex} + F_{intra}^{ex}\right) = 0 \quad (16)$$

We reiterate that the interlamellar repulsion has a Yukawa-type decay $\propto d^{-1}\, e^{-d/\lambda D}$ with lamellar distance, while the intralamellar free energy increases linearly with *d*. The balance between these two suggests the existence of an optimum spacing. Expressing all length scales in units of the nanosheet diameter *D*, we obtain:

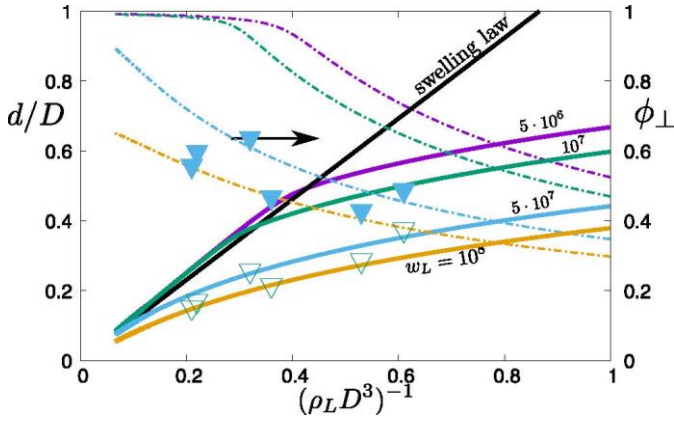

Fig. 10: Intralamellar distance d/λ_D versus the inverse nanosheet concentration, normalized in units of the nanosheet diameter D for a number of intralamellar repulsion amplitudes ω_L. The dash-dotted curves denote the corresponding intralamellar packing fraction $\phi_\perp$ plotted on the right vertical axis. The experimental data are indicated by the symbols (open triangles indicate *d*/*D*, filled ones $\phi_\perp$).

$$\pi l_B\lambda_D\omega_L\rho_L - \frac{8e^{-\frac{d}{\lambda_D}}}{\pi l_B\lambda_D\rho_L}\left(\frac{1}{d^2}+\frac{1}{\lambda_D d}\right) + \frac{1}{d}\left(\frac{1}{(\phi_\perp-1)^2}-1\right) = 0 \quad (17)$$

Note that the trivial ideal free energy of the lamellar phase is proportional to $\log\rho_L$ and does not depend on the intralamellar spacing. The results for the system under consideration are shown in Fig. 10. The spacings obtained from the "multistack" free energy Eq. (10) are very similar with values being only slightly larger for very concentrated samples ($\rho_LD^3 >> 1$). The trivial swelling law reads $d/D \approx (2/\sqrt{3})/\rho_LD^3$ and is recovered at larger nanosheet concentrations where the nanosheets are near close-packing. Away from this limit, the hard-core contribution has very little impact on the thermodynamics and may safely be neglected. For the concentration range probed in experiment ($\rho_LD^3 \approx 1$ - 5), the intralamellar structure turns out to be rather sparse with filling fractions of less than 50%, depending on the value of the intralamellar repulsion amplitude ω_L. The corresponding lamellar distances are about an order of magnitude smaller than those obtained from our modified DLVO theory (Section 4.1) and are in good agreement with the experimentally measured distances (100 – 300 nm), provided that the intralamellar repulsion $\omega_L \approx 10^8$ is taken about two orders of magnitude larger than the value that would ensue

from Eq. (15).[76] One possible explanation for the discrepancy is that the effective charge is larger than suggested by the naive scaling expression Eq. (13). The average edge-edge distance h between the sheets for typical intralamellar packing fraction of $\phi_\perp = 0.3$ is estimated to be $h/D \approx (4\phi_\perp/\pi)^{-1/2} - 1 \approx 0.6$ which amounts to h being about four to five times the Debye screening length. This may not be sufficiently large to reach the far-field regime in which the linearized DH description with renormalized surface potential should apply.[77] Furthermore, out-of-plane positional and orientational fluctuations of the nanosheets essentially disrupt the simple two-dimensional picture of the intralamellar fluid and enable the nanosheets to approach each other much more closely than the average diameter. This would render the contact distance $\sigma << D$, if not potentially zero.

4.5. Effect of polymer adsorption

The addition of low molecular weight (i.e. 100 kDa) polymer leads to adsorption onto the faces of the nanosheets (Fig. 6), resulting in nanosheets covered by a more-or-less uniform polymer coating. Even though there is a small fraction of free polymer in solution, the average separation between nanosheets is far too large for depletion forces to have any impact. Further, bridging forces due to simultaneous adsorption of a single polymer chain onto multiple nanosheets seem negligible as well. As far as the electrostatic properties are concerned, the main effect of the adsorbed polymer appears to be a drastic reduction of the bare nanosheet surface charge Z_{bare} (Fig. 7). Consequently, the Gouy-Chapman length $\ell_{\text{GC}} = (8\ell_B Z_{\text{bare}}\phi_\perp)^{-1}$ may reach a few hundred nanometers, reiterating that we keep the average nanosheet diameter D as our implicit length unit in all expressions. It is then conceivable that the interlamellar pressure no longer operates in the intermediate regime ($\ell_{\text{GC}} << \lambda_D$), but rather in the Debye-Hückel domain for weakly charged lamellae ($\ell_{\text{GC}} >> \lambda_D$) in which case the disjoining pressure reads:

$$\Pi_{DH} \sim \frac{2k_BT}{\pi l_B l_{GC}^2}\, exp\left(\frac{-d}{\lambda_D}\right) \qquad (18)$$

The same reasoning applies to the intralamellar free energy where Eq. (14) still holds but with the saturated effective charge replaced by the bare nanosheet charge. We may now simply repeat the free energy minimization from the previous paragraph to obtain the following condition for the lamellar distance, now assuming Debye-Hückel electrostatics for weakly charged nanosheets:

$$\frac{\pi}{64 l_B}\lambda_D\,\omega_0\rho_L - \frac{2\lambda_D e^{-\frac{d}{\lambda_D}}}{\pi\rho_L l_B}\left(\frac{1}{d^2}+\frac{1}{\lambda_D d}\right) + \frac{l_{GC}^2}{d}\left(\frac{1}{(\phi_\perp - 1)^2} - 1\right) = 0 \qquad (19)$$

where $\omega_0 = 4(y^{-1}I_1(y))^2\exp(-\sigma/\lambda_D)$ taking $\sigma = D$ for simplicity. The result in Fig. 11 demonstrates that the addition of polymer and the subsequent reduction of the nanosheet charge density caused by the polymer adsorption leads to a marked deswelling of the lamellar structure, in line with experimental observation.

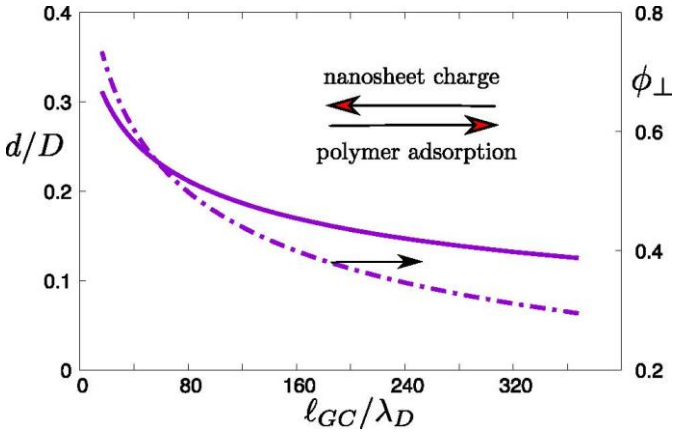

Fig. 11: Intralamellar distance d/λ_D from Debye-Hückel theory for the case of polymer adsorption reducing the nanosheet charge, as reflected by an increase of the Gouy-Chapman length ℓ_{GC} normalized by the Debye screening length λ_D. The overall nanosheet concentration was kept constant at $\rho_L D^3 = 3$. The dash-dotted curve denotes the corresponding intralamellar packing fraction $\phi_\perp$.

The case of high molecular weight (i.e. 1 MDa) polymer is obviously more complicated than that of the low molecular weight polymer modelled here because the trend experimentally observed in the former case is opposite to that of the latter. Then, a complete theoretical description should also involve an additional effective membrane repulsion related to the polymer coils in a way that we do not yet understand. Another speculative argument is that large polymers might induce bridging attraction between adjacent nanosheets within the same lamella. Then, at constant overall nanosheet concentration, such bridging attraction should decrease the intralamellar particle distance, which should in turn increase the lamellar period.

Furthermore, we wish to reiterate that the present theoretical model only applies to lamellar system; it does not take into consideration phase coexistence between lamellar and nematic or isotropic phases. This is a challenging issue that requires an appropriate thermodynamic description of (anisotropic) fluids of charged discotic colloids that remains largely elusive to date.[78,79]

5. Conclusions

The lamellar phase of $H_3Sb_3P_2O_{14}$ aqueous suspensions results from the self-assembly of the nanosheets in membranes that spontaneously organize in a periodic stack. In this work, we have shown that the particulate nature of the membranes is an essential ingredient required to understand the dependence on the nanosheet concentration of the lamellar period, hence the structural colour of the phase. Indeed, in this system, the usual DLVO approach based on infinite uniform lamellae fails to explain this dependence whereas our model that considers nanosheet-laden stacked lamellae provides a satisfactory semi-quantitative description of the data.

Moreover, we showed that adding PEO to the lamellar phase has an unexpected and spectacular effect on its structural colour. This effect is due to a change in lamellar spacing that decreases in the case of 100 kDa PEO but increases in the case of 1 MDa PEO. We found that PEO adsorbs on the nanosheets and therefore strongly reduces their negative charge. We argue that this is due to the Lewis-base character of the ethylene oxide repeat units that makes PEO positively charged at the low pH of the $H_3Sb_3P_2O_{14}$ suspensions, which is qualitatively confirmed by theoretical modelling. This interpretation is further supported by the fact that the same trend is observed with Dextran which also happens to have a Lewis-base character. Yet, the origin of the additional repulsion experienced by the nanosheet-laden membranes in presence of the 1 MDa PEO still remains unclear to date.

From a more applied point of view, our work shows how the structural colour of these 1-dimensional photonic materials can finely be tuned in the whole visible range not only by adjusting the nanosheet concentration but also by simply doping the phase with small amounts of polymer of carefully chosen molecular weight.

Conflicts of interest

There are no conflicts to declare.

Acknowledgements

Authors would like to thank (i) H. Lekkerkerker, P. van der Schoot, R. Podgornik, N. Miyamoto, E. Trizac, for helpful discussions; (ii) intern M. Le Meur for the bulk synthesis of $H_3Sb_3P_2O_{14}$; (iii) L. Cherni for TGA measurements; (iv) T. Bizien for assistance in using beamline SWING; (v) T. Narayanan, L. Sharpnack, and D. Constantin, for assistance in using beamline ID02. We also acknowledge SOLEIL for provision of synchrotron radiation facilities (under the approved proposal # 20181283) and ESRF for provision of synchrotron radiation facilities (under the approved proposal # SC-4867). JCG acknowledge funding from CEA's "Programme Transversal Nanoscience" and the European Research Council under the European Union's 7th Framework Program (FP/2007-2013)/ERC Grant Agreement N◦ [320915] "REE-CYCLE": Rare Earth Element reCYCling with Low harmful Emissions. KER, LM, JCG, PD acknowledge financial support from the "Agence Nationale de la Recherche" grant n°ANR-17-CE04-0003, project 4WATER.

References

1 U. Hofmann, K. Endell and D. Wilm, *Zeitschrift für Kristallographie - Crystalline Materials*, 1933, **86**, 340–348.
2 I. Langmuir, *J. Chem. Phys.*, 1938, **6**, 873–896.
3 T. Sasaki, M. Watanabe, H. Hashizume, H. Yamada and H. Nakazawa, *J. Am. Chem. Soc.*, 1996, **118**, 8329–8335.
4 T. Sasaki and M. Watanabe, *J. Am. Chem. Soc.*, 1998, **120**, 4682–4689.
5 N. Miyamoto and T. Nakato, *Adv. Mater.*, 2002, **14**, 1267-+.
6 T. Nakato and N. Miyamoto, *J. Mater. Chem.*, 2002, **12**, 1245–1246.
7 T. Nakato, N. Miyamoto, A. Harada and H. Ushiki, *Langmuir*, 2003, **19**, 3157–3163.
8 N. Miyamoto and T. Nakato, *J. Phys. Chem. B*, 2004, **108**, 6152–6159.
9 Z. Liu, R. Ma, Y. Ebina, N. Iyi, K. Takada and T. Sasaki, *Langmuir*, 2007, **23**, 861–867.
10 C. Valles, C. Drummond, H. Saadaoui, C. A. Furtado, M. He, O. Roubeau, L. Ortolani, M. Monthioux and A. Penicaud, *J. Am. Chem. Soc.*, 2008, **130**, 15802-+.
11 R. Ma and T. Sasaki, *Adv. Mater.*, 2010, **22**, 5082–5104.
12 N. Behabtu, J. R. Lomeda, M. J. Green, A. L. Higginbotham, A. Sinitskii, D. V. Kosynkin, D. Tsentalovich, A. N. G. Parra-Vasquez, J. Schmidt, E. Kesselman, Y. Cohen, Y. Talmon, J. M. Tour and M. Pasquali, *Nat. Nanotechnol.*, 2010, **5**, 406–411.
13 J. N. Coleman, M. Lotya, A. O'Neill, S. D. Bergin, P. J. King, U. Khan, K. Young, A. Gaucher, S. De, R. J. Smith, I. V. Shvets, S. K. Arora, G. Stanton, H.-Y. Kim, K. Lee, G. T. Kim, G. S. Duesberg, T. Hallam, J. J. Boland, J. J. Wang, J. F. Donegan, J. C. Grunlan, G. Moriarty, A. Shmeliov, R. J. Nicholls, J. M. Perkins, E. M. Grieveson, K. Theuwissen, D. W. McComb, P. D. Nellist and V. Nicolosi, *Science*, 2011, **331**, 568–571.
14 N. Miyamoto and T. Nakato, *Isr. J. Chem.*, 2012, **52**, 881–894.
15 V. Nicolosi, M. Chhowalla, M. G. Kanatzidis, M. S. Strano and J. N. Coleman, *Science*, 2013, **340**, 1420-+.
16 R. Ma and T. Sasaki, *Accounts Chem. Res.*, 2015, **48**, 136–143.
17 M. Stoeter, S. Rosenfeldt and J. Breu, in *Annual Review of Materials Research, Vol 45*, ed. D. R. Clarke, Annual Reviews, Palo Alto, 2015, vol. 45, pp. 129–151.
18 K. Kalantar-zadeh, J. Z. Ou, T. Daeneke, A. Mitchell, T. Sasaki and M. S. Fuhrer, *Appl. Mater. Today*, 2016, **5**, 73–89.
19 S. Rosenfeldt, M. Stoeter, M. Schlenk, T. Martin, R. Q. Albuquerque, S. Foerster and J. Breu, *Langmuir*, 2016, **32**, 10582–10588.

20 G. Bepete, E. Anglaret, L. Ortolani, V. Morandi, K. Huang, A. Penicaud and C. Drummond, *Nat. Chem.*, 2017, **9**, 347–352.

21 M. Daab, S. Rosenfeldt, H. Kalo, M. Stoeter, B. Bojer, R. Siegel, S. Foerster, J. Senker and J. Breu, *Langmuir*, 2017, **33**, 4816–4822.

22 M. Daab, N. J. Eichstaedt, C. Habel, S. Rosenfeldt, H. Kalo, H. Schiessling, S. Foerster and J. Breu, *Langmuir*, 2018, **34**, 8215–8222.

23 A. Gupta and S. Vasudevan, *J. Phys. Chem. C*, 2018, **122**, 19243–19250.

24 Y.-T. Xu, U. V. Mody and M. J. MacLachlan, *Nanoscale*, 2021, **13**, 7558–7565.

25 J. C. P. Gabriel, C. Sanchez and P. Davidson, *J. Phys. Chem.*, 1996, **100**, 11139–11143.

26 T. Nakato, N. Miyamoto and A. Harada, *Chem. Commun.*, 2004, 78–79.

27 L. J. Michot, I. Bihannic, S. Maddi, S. S. Funari, C. Baravian, P. Levitz and P. Davidson, *Proc. Natl. Acad. Sci. U. S. A.*, 2006, **103**, 16101–16104.

28 N. Miyamoto, H. Iijima, H. Ohkubo and Y. Yamauchi, *Chem. Commun.*, 2010, **46**, 4166–4168.

29 B. Dan, N. Behabtu, A. Martinez, J. S. Evans, D. V. Kosynkin, J. M. Tour, M. Pasquali and I. I. Smalyukh, *Soft Matter*, 2011, **7**, 11154–11159.

30 N. Miyamoto, S. Yamamoto, K. Shimasaki, K. Harada and Y. Yamauchi, *Chem.-Asian J.*, 2011, **6**, 2936–2939.

31 J. E. Kim, T. H. Han, S. H. Lee, J. Y. Kim, C. W. Ahn, J. M. Yun and S. O. Kim, *Angew. Chem.-Int. Edit.*, 2011, **50**, 3043–3047.

32 C. Zamora-Ledezma, N. Puech, C. Zakri, E. Grelet, S. E. Moulton, G. G. Wallace, S. Gambhir, C. Blanc, E. Anglaret and P. Poulin, *J. Phys. Chem. Lett.*, 2012, **3**, 2425–2430.

33 A. F. Mejia, Y.-W. Chang, R. Ng, M. Shuai, M. S. Mannan and Z. Cheng, *Phys. Rev. E*, 2012, **85**, 061708.

34 E. Paineau, A. M. Philippe, K. Antonova, I. Bihannic, P. Davidson, I. Dozov, J. C. P. Gabriel, M. Imperor-Clerc, P. Levitz, F. Meneau and L. J. Michot, *Liq. Cryst. Rev.*, 2013, **1**, 110–126.

35 Z. Xu and C. Gao, *Accounts Chem. Res.*, 2014, **47**, 1267–1276.

36 F. Chen, M. Chen, Y.-W. Chang, P. Lin, Y. Chen and Z. Cheng, *Soft Matter*, 2017, **13**, 3789–3793.

37 A. P. Draude and I. Dierking, *Crystals*, 2019, **9**, 455.

38 M. Zeng, D. King, D. Huang, C. Do, L. Wang, M. Chen, S. Lei, P. Lin, Y. Chen and Z. Cheng, *Proc. Natl. Acad. Sci. U. S. A.*, 2019, **116**, 18322–18327.

39 J. C. P. Gabriel, F. Camerel, B. J. Lemaire, H. Desvaux, P. Davidson and P. Batail, *Nature*, 2001, **413**, 504–508.

40 P. Davidson, C. Penisson, D. Constantin and J.-C. P. Gabriel, *Proc. Natl. Acad. Sci. U. S. A.*, 2018, **115**, 6662–6667.

41 D. Sun, H.-J. Sue, Z. Cheng, Y. Martinez-Raton and E. Velasco, *Phys. Rev. E*, 2009, **80**, 041704.

42 K. Sano, Y. S. Kim, Y. Ishida, Y. Ebina, T. Sasaki, T. Hikima and T. Aida, *Nat. Commun.*, 2016, **7**, 12559.

43 F. Geng, R. Ma, A. Nakamura, K. Akatsuka, Y. Ebina, Y. Yamauchi, N. Miyamoto, Y. Tateyama and T. Sasaki, *Nat. Commun.*, 2013, **4**, 1632.

44 M. Wong, R. Ishige, T. Hoshino, S. Hawkins, P. Li, A. Takahara and H.-J. Sue, *Chem. Mat.*, 2014, **26**, 1528–1537.

45 D. Yamaguchi, N. Miyamoto, T. Fujita, T. Nakato, S. Koizumi, N. Ohta, N. Yagi and T. Hashimoto, *Phys. Rev. E*, 2012, **85**, 011403.

46 K. Szendrei, P. Ganter, O. Sanchez-Sobrado, R. Eger, A. Kuhn and B. V. Lotsch, *Adv. Mater.*, 2015, **27**, 6341-6348.

47 W. Yang, S. Yamamoto, K. Sueyoshi, T. Inadomi, R. Kato and N. Miyamoto, *Angew. Chem.-Int. Edit.*, , DOI:10.1002/anie.202015982.

48 K. Shimasaki, T. Yamaki, S. Sawada, A. Hiroki, Y. Maekawa and N. Miyamoto, *J. Nanosci. Nanotechnol.*, 2016, **16**, 9231–9237.

49 N. Yamaguchi, S. Anraku, E. Paineau, C. R. Safinya, P. Davidson, L. J. Michot and N. Miyamoto, *Sci Rep*, 2018, **8**, 4367.

50 K. El Rifaii, H. H. Wensink, T. Bizien, J.-C. P. Gabriel, L. Michot and P. Davidson, *Langmuir*, 2020, **36**, 12563–12571.

51 Y. Martinez-Raton and E. Velasco, *J. Chem. Phys.*, 2011, **134**, 124904.

52 Y. Piffard, A. Verbaere, A. Lachgar, S. Deniardcourant and M. Tournoux, *Revue De Chimie Minerale*, 1986, **23**, 766–775.

53 T. Narayanan, M. Sztucki, P. Van Vaerenbergh, J. Leonardon, J. Gorini, L. Claustre, F. Sever, J. Morse and P. Boesecke, *J. Appl. Crystallogr.*, 2018, **51**, 1511–1524.

54 L. A. Feigin and D. I. Svergun, *Structure Analysis by Small-Angle X-Ray and Neutron Scattering*, Springer US, Boston, MA, 1987.

55 J. D. Joannopoulos, S. G. Johnson, J. N. Winn and R. D. Meade, *Photonic Crystals: Molding the Flow of Light - Second Edition*, Princeton University Press, 2011.

56 T. L. Kuhl, D. E. Leckband, D. D. Lasic and J. N. Israelachvili, *Biophysical Journal*, 1994, **66**, 1479–1488.
57 K. Devanand and J. C. Selser, *Macromolecules*, 1991, **24**, 5943–5947.
58 C. Liu, K. K. Ewert, E. Wonder, P. Kohl, Y. Li, W. Qiao and C. R. Safinya, *ACS Appl. Mater. Interfaces*, 2018, **10**, 44152–44162.
59 G. Fleer, M. A. C. Stuart, J. M. H. M. Scheutjens, T. Cosgrove and B. Vincent, *Polymers at Interfaces*, Springer Netherlands, 1998.
60 J. Swenson, M. V. Smalley, H. L. M. Hatharasinghe and G. Fragneto, *Langmuir*, 2001, **17**, 3813–3818.
61 S. Mathur and B. M. Moudgil, *Journal of Colloid and Interface Science*, 1997, **196**, 92–98.
62 B. Fei and Q. Shen, *J. Macromol. Sci. Part A-Pure Appl. Chem.*, 2018, **55**, 611–617.
63 E. J. W. Verwey, J. T. G. Overbeek and K. van Nes, *Theory of the Stability of Lyophobic Colloids: The Interaction of Sol Particles Having an Electric Double Layer*, Elsevier Publishing Company, 1948.
64 D. Andelman, in *Handbook of Biological Physics*, Elsevier, 1995, vol. 1, pp. 603–642.
65 E. Trizac and J. P. Hansen, *Phys. Rev. E*, 1997, **56**, 3137–3149.
66 R. J. F. Leote de Carvalho, E. Trizac and J. P. Hansen, *Europhys. Lett.*, 1998, **43**, 369–375.
67 P. Pincus, J. Joanny and D. Andelman, *Europhys. Lett.*, 1990, **11**, 763–768.
68 T. Odijk, *Langmuir*, 1992, **8**, 1690–1691.
69 R. de Vries, J. Phys. II (France), 1994, 4, 1541.
70 M. Kiometzis and H. Kleinert, *Phys. Lett. A*, 1989, **140**, 520–524.
71 J. Harden, C. Marques, J. Joanny and D. Andelman, *Langmuir*, 1992, **8**, 1170–1175.
72 H. Reiss, H. Frisch and J. Lebowitz, *J. Chem. Phys.*, 1959, **31**, 369–380.
73 E. Helfand, H. Reiss, H. Frisch and J. Lebowitz, *J. Chem. Phys.*, 1960, **33**, 1379–1385.
74 J.-P. Hansen and I. R. McDonald, *Theory of simple liquids*, Elsevier / Academic Press, Amsterdam ; Boston, 3rd ed., 2007.
75 E. Trizac, L. Bocquet, R. Agra, J. J. Weis and M. Aubouy, *J. Phys.-Condens. Matter*, 2002, **14**, 9339–9352.
76 The discrepancy could be accounted for by testing the effective Debye-Hückel potential Eq. (12) against a full numerical solution of the 3D nonlinear Poisson-Boltzmann equation for two highly charged parallel circular discs in a coplanar configuration. This goes beyond the scope of the present work.
77 L. Bocquet, E. Trizac and M. Aubouy, *J. Chem. Phys.*, 2002, **117**, 8138–8152.
78 D. G. Rowan and J. P. Hansen, *Langmuir*, 2002, **18**, 2063–2068.
79 L. Harnau, *Mol. Phys.*, 2008, **106**, 1975–2000.

Table of Contents Graphic

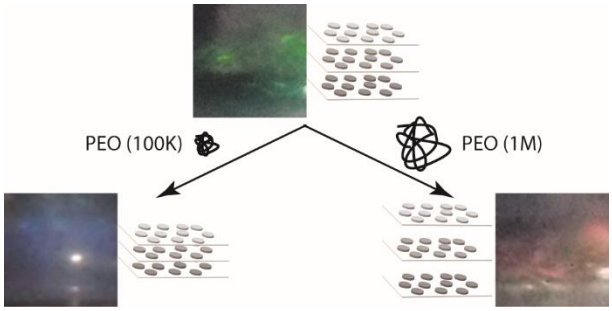

Doping a photonic lamellar mesophase of mineral nanosheets with low (resp. high) molecular weight PEO shifts its colour from green to blue (resp. red).